Dynamic earthquake rupture in the lower crust

Arianne Petley-Ragan, Yehuda Ben-Zion, Hakon Austrheim, Benoit Ildefonse, Francois Renard, Bjorn Jamtveit

GEOPHYSICS

Dynamic earthquake rupture in the lower crust

Arianne Petley-Ragan[1]*, Yehuda Ben-Zion[2], Håkon Austrheim[1], Benoit Ildefonse[3], François Renard[1,4], Bjørn Jamtveit[1]

Earthquakes in the continental crust commonly occur in the upper 15 to 20 km. Recent studies demonstrate that earthquakes also occur in the lower crust of collision zones and play a key role in metamorphic processes that modify its physical properties. However, details of the failure process and sequence of events that lead to seismic slip in the lower crust remain uncertain. Here, we present observations of a fault zone from the Bergen Arcs, western Norway, which constrain the deformation processes of lower crustal earthquakes. We show that seismic slip and associated melting are preceded by fracturing, asymmetric fragmentation, and comminution of the wall rock caused by a dynamically propagating rupture. The succession of deformation processes reported here emphasize brittle failure mechanisms in a portion of the crust that until recently was assumed to be characterized by ductile deformation.

INTRODUCTION

An increasing number of studies indicate that the structural and metamorphic evolution of the lower crust during an orogenic event involves an early stage of seismic failure (*1*–*7*). Microstructural observations show that the incipient stages of metamorphism and associated rheological weakening are associated with the introduction of fluids into fragmented fault wall rocks. Fragmentation without notable shear strain and the development of asymmetric "feather features" around microscopic shear fractures furthermore suggest the development of dynamic stress levels far beyond lithostatic (*6*). The mechanisms producing earthquakes in the lower crust are still not understood. Alternative explanations include shear caused by thermal runaway instabilities (*8*, *9*), fluid-induced failure (*10*), instabilities triggered by metamorphic transformation processes (*11*, *12*), stress transfer during local reaction-induced weakening (*4*), and aftershocks of large earthquakes in the shallower seismogenic regime (*5*).

Here, we describe in detail the internal structure of a lower crustal earthquake rupture zone from the Bergen Arcs in western Norway by the use of x-ray computed microtomography, electron backscatter diffraction (EBSD), and grain size analysis. The observations provide direct evidence that the fault was initiated by brittle dynamic rupture and that rock fragmentation and asymmetric damage near and behind the rupture front predated subsequent frictional sliding and associated melting. The process that allowed aqueous fluids to enter the wall rocks, which triggered the incipient metamorphic and structural changes of this crustal volume, may thus have been very short lived.

RESULTS

Field observations and microstructures

The fault is located on the northwestern portion of the island of Holsnøy in the Lindås Nappe of the Bergen Arcs where plagioclase-rich granulite facies anorthosite [ca. 930 million years (Ma)] was locally metamorphosed at amphibolite to eclogite facies conditions (ca. 420 to 430 Ma) in spatial relation to faults and shear zones (fig. S1A) (*13*, *14*). The fault is oriented 265/70°N and intersects the granulite facies foliation (115/80°SW) at 30° (fig. S1B). The fault displays an apparent offset of a garnet-pyroxene seam of 1.7 m (fig. S1C). Wall rock damage is locally evident as a light-colored wedge-shaped zone on the northern side of the fault where the granulite facies foliation has been largely obliterated (Fig. 1A). The damage zone thickness increases eastward to ca. 6 cm over an observable length of 40 cm. The wall rock opposite of the damage zone is fractured with fine-grained alteration products but still preserves the original granulite foliation (fig. S2). Pseudotachylyte injection veins extend from the fault core into the damage zone but do not extend further into the northern wall rock nor are they present in the southern wall rock. Injection veins are not present along the fault outside of the asymmetrical damage zone (fig. S1D). East of the damage zone, the fault and wall rock have equilibrated at amphibolite facies conditions. A patch, with traceable boundary, of pervasive retrogressed granulite protolith to amphibolite facies assemblage overprints the fault without offset (fig. S1D).

The fault core to the west of the damage zone consists of a zoned pseudotachylyte (8 mm thick) bounded on both sides by foliated cataclasite (Fig. 1, B and D). The fault core adjacent to the damage zone also includes a zoned pseudotachylyte (14 mm thick), but cataclasites are absent (Fig. 1C). The inner pseudotachylyte along the entire fault contains plagioclase microlites with Na zoning, clinozoisite symplectites with quartz, and microcrystalline kyanite, hornblende, K-feldspar, and anorthite (fig. S3, A and B). Adjacent to the damage zone, the inner pseudotachylyte contains less plagioclase (fig. S3C), while the number of plagioclase wall rock clasts is greater. Bands of aligned clinozoisite symplectites run parallel to the strike of the fault within the inner pseudotachylyte (Fig. 1B and fig. S3A). The outer pseudotachylyte ranges from microcrystalline plagioclase and hornblende (fig. S3D) to crystalline plagioclase, anorthite, and hornblende (fig. S3E). Kyanite, K-feldspar, quartz, biotite, and dolomite are also found within the outer pseudotachylyte along with rare dendritic grossular-rich garnet (fig. S3, A and E). The dendritic garnet and plagioclase with primary zoning most likely crystallized directly from the frictional melt; however, the presence of hydrous and carbonate mineral phases within the pseudotachylyte suggests partial equilibration at amphibolite facies. The conditions of equilibration based on the mineral assemblage in the outer pseudotachylyte (Fig. 1B) are estimated to 0.9 to 1.0 GPa and 550° to 625°C [figure 2B of (*15*)]. Directly east of the damage zone,

[1]Physics of Geological Processes, The Njord Centre, University of Oslo, Oslo, Norway. [2]Department of Earth Sciences, University of Southern California, Los Angeles, CA, USA. [3]Géosciences Montpellier, CNRS, University of Montpellier, Université des Antilles, Montpellier, France. [4]University Grenoble Alpes, University Savoie Mont Blanc, CNRS, IRD, IFSTTAR, ISTerre, Grenoble, France.
*Corresponding author. Email: a.j.petley-ragan@geo.uio.no

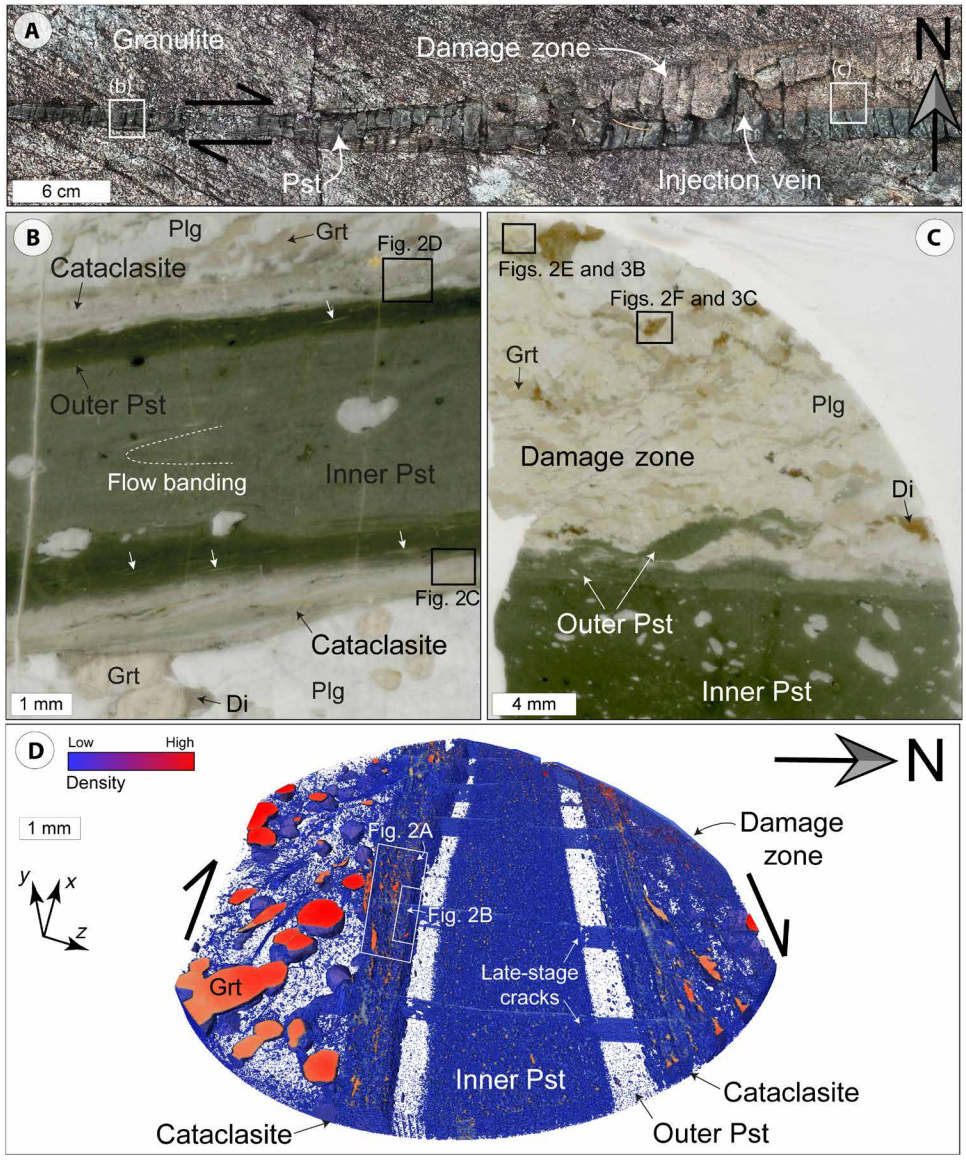

Fig. 1. Structure of the lower crustal fault in the Bergen Arcs. (**A**) The damage zone is present on the northern side of the fault and is locally intruded by injection veins branching from the pseudotachylyte (Pst). (**B**) The interior of the fault consists of a zoned pseudotachylyte (inner and outer pseudotachylyte) bounded by cataclasites. The wall rock contains garnet (Grt), plagioclase (Plg), and diopside (Di). Clasts of cataclasite have been entrained in the outer pseudotachylyte (white arrows). (**C**) The damage zone contains fragmented wall rock minerals with little to no shear strain. Along this portion of the fault, cataclasites are absent. North is up in (B) and (C). (**D**) X-ray computed microtomography image of the fault shown in (B). The outer pseudotachylyte and wall rock plagioclase are transparent for better three-dimensional rendering. The orientation of the reference frame is as follows: *x*, west; *y*, perpendicular to the topographic surface; and *z*, north. Photo credit: (A, B, and C) Arianne Petley-Ragan, University of Oslo and (D) Francois Renard, University of Oslo.

the pseudotachylyte is fully equilibrated at amphibolite facies (fig. S4A). Large crystals of clinozoisite are randomly oriented in association with plagioclase and kyanite within the fault core, and clast pseudomorphs are aggregates of paragonite, albite, and clinozoisite (fig. S4B).

Clasts of cataclasite float within the outer pseudotachylyte (Fig. 1B). The cataclasites are 50 to 60% plagioclase-rich matrix (<0.1 mm) with garnet, plagioclase, and diopside clasts (Fig. 2, A to D). Other matrix phases include hornblende, kyanite, quartz, K-feldspar, clinozoisite, and minor biotite and carbonates. The cataclasite foliation is defined by elongated aggregates of clast fragments. Garnet clasts show overgrowth by new grossular-rich garnet near the outer pseudotachylyte (fig. S5A), and diopside clasts display Na-rich growth rims (mineral compositions are presented in table S1 and fig. S6). The amount of garnet growth is noticeably greater in the northern cataclasite than in the southern cataclasite. The contact between the cataclasites and the outer pseudotachylyte is defined by long aggregates of small garnet fragments with growth rims creating a strong lineation (Fig. 2, B to D, and fig. S5B). The ellipticity of the aggregates gives a minimum shear strain of 5 to 7 and a dextral sense of shear (see the "Image analysis of garnet clasts" section). The direction of slip was measured by the orientation of garnet aggregates at an angle of 31° from the topographic surface, providing an estimate for the

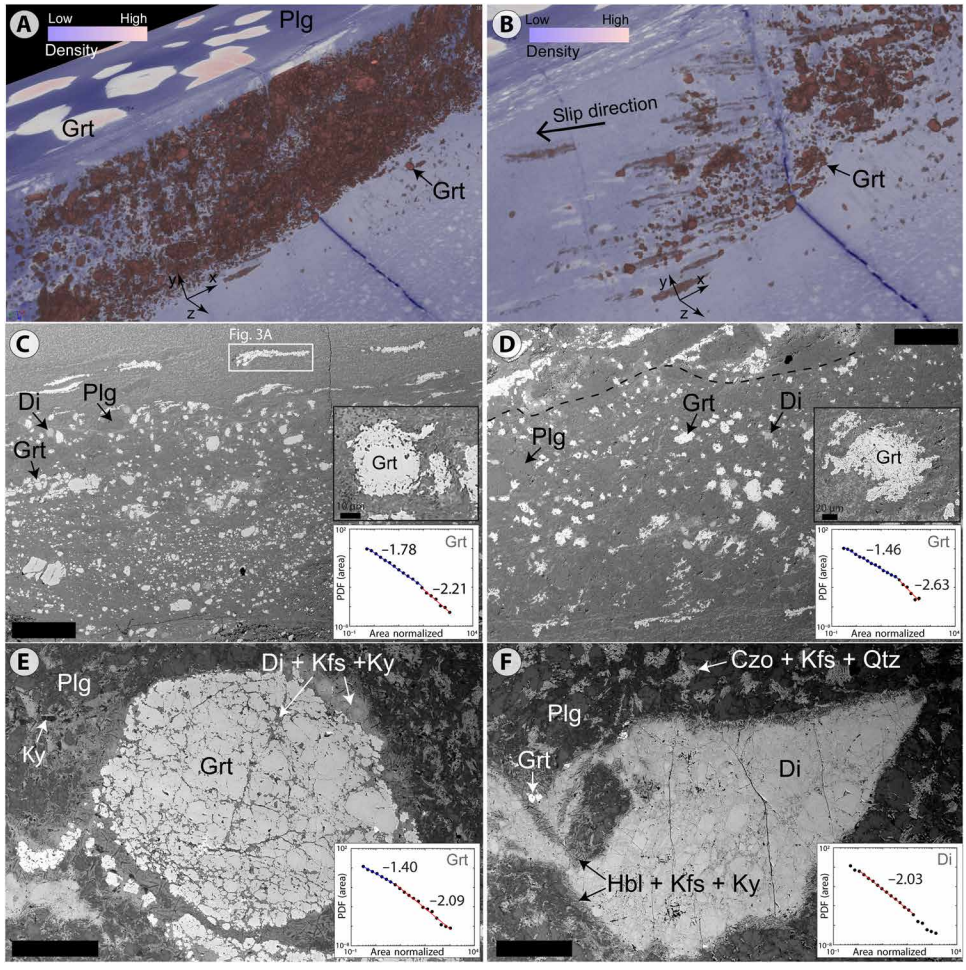

Fig. 2. Microstructures in the cataclasites and damage zone. (**A** and **B**) Three-dimensional x-ray computed microtomography images looking southwest showing extracted garnet clasts (Grt) in the cataclasite (dark red). The entire volume of the cataclasite is shown in (A), and the volume adjacent to the outer pseudotachylyte is shown in (B). The *x-y-z* coordinate system is the same as in Fig. 1D. (**C** and **D**) Backscatter electron (BSE) images of the (C) southern and (D) northern cataclasite. The boundary with the outer pseudotachylyte is marked by elongated aggregates of garnet fragments with growth rims. Insets show garnet clasts with growth rims and the grain size distribution [probability density function (PDF)] of garnet clasts with associated power law exponents (see Methods). (**E** and **F**) BSE images of the (E) fragmented garnet and (F) fragmented diopside (Di) in the damage zone. Fragmented garnet has a corona of diopside, K-feldspar (Kfs), and kyanite (Ky). Fragmented diopside has a corona of hornblende (Hbl), K-feldspar, and kyanite. Note the fragmented plagioclase (Plg) with clinozoisite (Czo), K-feldspar, kyanite, and quartz (Qtz) growth (see also fig. S7). Insets show the grain size distribution of garnet and diopside clasts with associated power law exponents. Scale bars, 0.25 mm. North is up in (C) to (F). Photo credit: (A and B) Benoit Cordonnier, University of Oslo; (C) through (F), Arianne Petley-Ragan.

actual total offset for the fault to ca. 2 m (see the "High-resolution x-ray microtomography" section). The garnet clasts away from the pseudotachylyte contact in the cataclasites reveal a size (area) distribution with power law exponents of ca. −1.5 and −1.8 and a crossover to steeper slopes (−2.2 and − 2.6) for the largest clasts [insets of Fig. 2, C and D; see (*16*) and Methods].

Plagioclase, diopside, and garnet are highly fragmented in the damage zone, but most microfractures do not display any shear offset of the cross-cut grain boundaries. The coronae of diopside, K-feldspar, and kyanite surround the fragmented garnet grains and also occur as inclusions in the fragmented garnets (Fig. 2E). Likewise, fragmented diopside grains contain coronae of hornblende, K-feldspar, and kyanite (Fig. 2F) and inclusions of K-feldspar, quartz, and sometimes grossular-rich garnet. Fragmented plagioclase is pervasively overgrown by randomly oriented clinozoisite, K-feldspar, quartz, and kyanite (fig. S7). Grossular-rich garnet neoblasts and carbonates are locally present within the damaged plagioclase domains.

EBSD (see Methods) was used to obtain the crystallographic orientations of an elongated aggregate of garnet fragments in the southern cataclasite and two fragmented grains in the damage zone. The aggregate of garnet fragments with growth rims near the boundary to the pseudotachylyte (Fig. 2C) displays a uniform distribution of crystallographic orientations and high-angle misorientations (Fig. 3A and fig. S8A). The fragmented garnet in the damage zone (Fig. 2E) displays a strong crystallographic-preferred orientation (CPO) in the upper part of the map where low-angle boundaries are abundant (Fig. 3B and fig. S8B). The bottom half of the map displays weakly rotated fragments bounded by high-angle boundaries. The fragmented diopside (Fig. 2F) also displays a strong CPO and a high number of low-angle boundaries (Fig. 3C and fig. S8C). The misorientation distributions of microstructures in the damage zone are skewed to the right and illustrate the limited amount of shear strain experienced by both the original garnet and diopside grain. This is in sharp contrast to the uniform misorientation distribution and

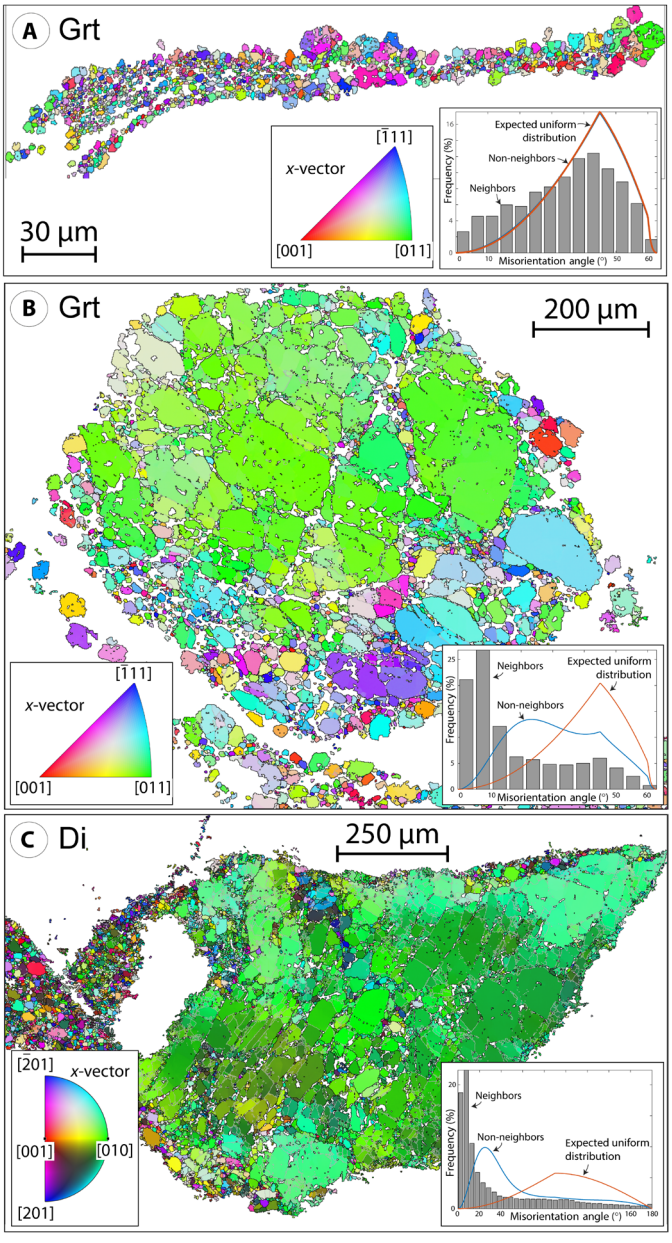

Fig. 3. Microstructures in the cataclasites and damage zone. EBSD results for (**A**) an elongated aggregate of garnet fragments in the cataclasite (Fig. 2C), (**B**) garnet in the damage zone (Fig. 2E), and (**C**) diopside in the damage zone (Fig. 2F). Grain boundaries (≥10°) are black, and low-angle boundaries (1° to 9°) are gray. Orientation maps use inverse pole figure coloring in relation to the *x*-vector (horizontal in image). Insets display the distribution of misorientations for neighboring (gray bars) and non-neighboring (blue line) grains compared with an expected uniform distribution (orange line).

extensive shear strain experienced by garnet grains in the cataclasites near the boundary to the outer pseudotachylyte. The size (area) distributions of subgrains and grains obtained by EBSD reveal power law relations with exponents near −2 (insets of Fig. 2, E and F, and fig. S9). For the garnet in the damage zone, there is a cross-over to a power law exponent of −1.4 for small clast sizes.

Temporal evolution of failure processes

The observations described above provide tight constraints on the mechanical and thermal evolution of this lower crustal fault. Asymmetric brittle fragmentation of the wall rocks with very limited shear strain is similar to observations associated with damage and pulverization of wall rocks around faults in the shallow seismogenic crust (*17*–*19*) and near the brittle-ductile transition (*20*). The scaling properties of the garnet and diopside fragment size distribution is also similar to what has been described from pulverized rocks around shallow faults (an exponent of −2 for the area distribution corresponds to an exponent of −3 for the radius distribution). These distributions have previously been ascribed to fragmentation involving rapid volumetric expansion and contraction (*21*–*23*).

Abundant clasts and cataclasite within the pseudotachylyte (Fig. 1, B and C) and injection of frictional melt (represented by pseudotachylyte veins) into the damage zone (Fig. 1, A and C) indicate that fracturing, fragmentation, and comminution predate melting. This is consistent with experimental results (*24*) and previous field observations (*25*–*27*). In this scenario, the initial stage of faulting involved intense brittle deformation focused around a propagating rupture front (*28*), with cracking and fragmentation that locally reaches up to 6 cm into the wall rock on the northern side of the fault. Localization of shear strain within the fault core then generated foliated cataclasites, with garnet clast size distributions similar to what is expected from a brittle comminution process with a power law exponent of ≥−1.8 corresponding to ≥−2.6 for the radius distribution (*29*, *30*).

Shear heating with accumulation of slip behind the propagating front (*31*) led to frictional melting of the brittle damage products. The thickening of the pseudotachylyte and the disappearance of the cataclasites adjacent to the damage zone (Fig. 1C) support a higher degree of melting where the wall rock was more fragmented. The large volume of melt directly adjacent to the damage zone eventually led to the pressurized injection of frictional melt into the damaged wall rock (Fig. 1, A and C). Increased porosity and permeability generated by brittle deformation permitted subsequent aqueous fluid introduction and incipient metamorphism of the pseudotachylyte to form hydrous mineral phases (i.e., clinozoisite symplectites; fig. S3B), of the cataclasites to form growth rims around clasts (Fig. 2, C and D), and of the damaged wall rock to form coronae around fragmented grains (Fig. 2, E and F). The extensive damage experienced by the northern wall rock resulted in greater fluid infiltration and metamorphic growth in the northern cataclasite and damage zone as compared with the southern side.

Figure 4 illustrates the temporal evolution of the Bergen Arc fault according to our field and microstructural observations. (i) Initial fragmentation with minimal shear occurred in the process zone around the rupture tip and extended into one wall rock. (ii) This was followed by comminution and grinding of the fragments with increasing shear motion behind the tip in the fault core. (iii) As shear heating progressed with slip accumulation further behind the propagating tip, the cataclasites began to melt with higher melt fractions in locations with greater volume of damaged wall rock. Last, (iv) fluid infiltration and metamorphism modified the mineralogy and microstructures on a longer post-seismic timescale.

DISCUSSION

Dynamic rupture propagation

The observed fault structure and temporal evolution are consistent with propagation of a dynamic shear rupture that produces symmetric fracturing at the rupture tip (the process zone), asymmetric cracking and fragmentation of the wall rock (the damage zone), and shear

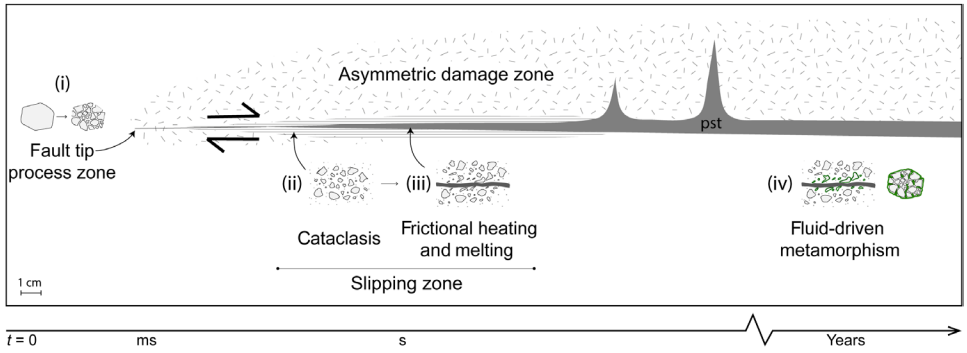

Fig. 4. Temporal evolution of deformation processes in the fault. The fault propagates from right to left, and the time since the rupture tip passed increases to the right. The illustration is based on a rupture zone with clear damage and melting products observed in the field (Fig. 1A). (**i**) Fragmentation occurs near the rupture tip and into one wall rock. (**ii**) Dextral shear motion concentrates within the rupture zone behind the tip, and the damaged rock undergoes cataclasis. (**iii**) Accumulation of shear motion within the cataclasites leads to frictional heating and melting. Melt products are injected into the damage zone, and cataclasites are completely melted where the volume of the damaged wall rock is greatest. (**iv**) Metamorphism (green) creates secondary phases in the pseudotachylyte, growth rims around the clasts in the cataclasites, and coronae around fragmented grains in the damage zone. Differential cooling of the pseudotachylyte to create zoned veins is not included in the illustration.

motion in the region behind the front (the slipping zone) (*32*–*35*). The asymmetric damage zone indicates that the fault was generated by a single one-directional rupture (propagating to the left in Fig. 1A), with damage prominent on the side (northern portion of the fault in Fig. 1A) subjected to tensile dynamic stress (*34*–*36*).

Initial fragmentation within the process zone involves stresses considerably higher than lithostatic pressure (*33*, *37*). Microstructures indicative of high stress conditions have recently been documented around faults from other localities on Holsnøy (*6*). Behind the rupture tip, opposing stress fields of tensile and compressive domains are created on either side of the slipping zone (*32*). Since rocks are weaker under tension, inelastic deformation in the form of tensile cracks takes place on only one side of the rupture (*38*, *39*). A reduction of elastic moduli in cracked regions produces damage-related radiation with strong isotropic component (*40*), which contributes to further fragmentation of the wall rock with minimal shear strain (i.e., pulverization).

The "wake" of cracked and fragmented rock behind the propagating tip was subjected to shear motion and wear mechanisms (i.e., sliding and rolling of fragments, and asperity collisions) that produced cataclasites and, as temperatures increased, melt products. The production of fine-grained cataclasite in the slipping zone would provide ideal conditions for melting (*24*, *41*). Melting of the cataclasites began with the disappearance of garnet and diopside at the boundary to the outer pseudotachylyte (Fig. 2, C and D), indicating frictional temperatures exceeding 1200°C and possibly a thermal shock of these phases (*42*). The fragmented rock generated through dynamic rupture produced the necessary starting material for a shear melting process behind the propagating front.

Implications for dynamic rupture in the lower crust

The observations described above emphasize the role of dynamic fracturing during brittle failure of the lower crust. The front of a propagating earthquake rupture in the lower crust is then followed by accumulation of slip and frictional melting. Local asymmetric fragmentation without notable shear strain can hardly be explained by viscous mechanisms, which are expected to produce symmetric wall rock structures along the entire length of a fault. Using empirical regression relations (*43*) and assuming that the 2 m displacement represents either the maximum or average slip of both strike-slip and reverse faults, the analyzed lower crustal earthquake had a magnitude of 6.9 ± 0.3 and a corresponding rupture length of 57 ± 26 km. However, uncertainty remains about whether these scaling relations are applicable to lower crustal earthquakes. These values, combined with statistical scaling results for earthquakes, indicate that the radiated seismic energy from the event was ~5×10^9 MJ [figure 6 of (*44*)]. This radiated energy likely produces additional brittle fracturing (i.e., aftershocks), increased permeability, and associated fluid-induced metamorphic changes in a substantial volume around the earthquake rupture zone.

The extent of asymmetrical off-fault damage by a dynamic rupture reflects the peak normal stress produced in the process zone and in the tensile quadrant of the slipping zone (*34*, *35*). The peak normal stress is proportional to the length of the slipping zone, proportional to the stress drop divided by the strength drop, and inversely proportional to the rupture velocity (*32*, *40*, *45*). The rupture likely propagated as a pulse with an approximately constant slipping zone length because of either annealing behind the front due to pseudotachylyte crystallization or dynamic changes of normal stress (*46*). Therefore, with a constant slipping zone length, the local development of thick asymmetrical damage zones represents a deceleration of the rupture. This may arise if the rupture tip passes through geometrical or material heterogeneity along its path. In this respect, asymmetric macroscopic damage zones are not expected along the entire length of dynamic rupture faults in the lower crust; only when the right conditions are met that the extent of off-fault damage becomes sufficient to produce these features macroscopically [figure 1A of this paper and Fig. 1B of (*47*)].

The width of asymmetrical damage zones is predicted to decrease with increasing confining stress (*34*, *35*, *45*). Hence, earthquake-generated damage zones will become narrower with increasing depth such that, in the lower crust, they will typically be centimeter scale or less, as observed in the Bergen Arcs. This may explain why most of pseudotachylyte-bearing faults from lower crustal rocks are not associated with thick asymmetrical damage zones but more often describe asymmetric injections of pseudotachylyte veins (*36*). On the other hand, damage-related radiation increases in amplitude with increasing confining stress (*40*), suggesting that there is a greater

potential for rock fragmentation with increasing depth. Asymmetrical lower crustal damage zones with the different components described in this paper may either be commonly overlooked in the field, be too thin to be observed, or become completely incorporated into the melt during subsequent frictional sliding. Furthermore, they may be consumed by shear localization that may erase any evidence of the initial fragmentation stage caused by dynamic rupture propagation. A neighboring fault to the one studied here displays such a scenario in which shear strain is localized within an asymmetrical damage zone (fig. S10).

The sequence of events illustrated in Fig. 4 reflects how processes operating at very different timescales leave their imprint in the rock structures and microstructures. Stress pulses lasting for microseconds cause a fragmentation process that precedes shear strain, while the subsequent frictional heating that causes melting may last seconds to tens of seconds (*47*). Metamorphic reactions in the pseudotachylyte, cataclasites, and wall rocks are driven by fluid infiltration in the wake of fracturing and permeability generation and most likely require weeks to years to crystallize the reaction products at the micrometer to millimeter scale. Only then, the weakening caused by the grain size reduction and formation of hydrous minerals allows ductile deformation mechanisms to generate the lower crustal shear zones that have frequently been described from this part of the Bergen Arcs.

METHODS

Image analysis of garnet clasts

A Hitachi SU5000 field emission scanning electron microscope at the University of Oslo's Department of Geosciences was used to obtain photomicrographs of the cataclasites. The short and long axes of the elongated garnet aggregates were measured from backscatter electron (BSE) images (e.g., Fig. 2, C and D). The shear strain in the cataclasite was then determined on the basis of the mean ellipticity of the aggregates. Grain size distributions of garnet clasts were obtained by isolating the grayscale of the BSE images for garnet. Objects less than 30 pixels and those that intersected the image border were removed. Six images of the southern cataclasite with a total of 7580 garnets and four images of the northern cataclasite with a total of 1995 garnets were used. Some of the garnet clasts from the images showed minor growth along their rims. The grain size distributions were fitted with either one or two power laws following the same procedure as in (*16*).

EBSD analysis

A CamScan X500FE Crystal Probe equipped with an Oxford/Nordlys EBSD detector at Géosciences Montpellier at the University of Montpellier in France was used to obtain the crystallographic orientations of the elongated aggregate of garnet fragments with growth rims in the cataclasite (Fig. 3A) and the fragmented garnet and diopside in the damage zone (Fig. 3, B and C). The EBSD was run with an accelerating voltage of 18 to 20 kV, a sample tilt of 70°, and a working distance of 25 mm. A step size of 0.4 μm was used for the aggregate of garnet fragments, and a step size of 1 μm was used for both the fragmented garnet and diopside grains. The MATLAB toolbox MTEX (version 5.1.1) was used to construct the EBSD maps and perform grain analysis. Grains and subgrains less than 3 to 5 μm were removed. A total of 1083 grains from the sheared garnet aggregate, a total of 3554 subgrains and grains from the fragmented garnet, and a total of 10,861 subgrains and grains from the fragmented diopside were used to obtain grain size distributions. The grain size distributions were fitted with either one or two power laws following the same procedure as in (*16*).

High-resolution x-ray microtomography

An x-ray tomography scan of the core sample was acquired at the European Synchrotron Radiation Facility, beamline ID19, with a voxel size of 6.5 μm and an energy of 92 keV. Data processing and three-dimensional (3D) rendering were performed using the software AvizoFire. The images in Figs. 1D and 2 (A and B) were colored by density. The outer pseudotachylyte in Fig. 1D was made transparent for better 3D rendering. The direction of elongation of garnets at the boundary between the cataclasite and outer pseudotachylyte allowed for the estimation of a slip direction and an angle of 31° from the topographic surface. This allowed for the calculation of the actual offset of 2 m based on an apparent offset of 1.7 m measured in the field (fig. S1C).

SUPPLEMENTARY MATERIALS

Supplementary material for this article is available at http://advances.sciencemag.org/cgi/content/full/5/7/eaaw0913/DC1

Fig. S1. Field structures of the fault in the Bergen Arcs.
Fig. S2. Images of damage in the southern wall rock.
Fig. S3. Microstructures of the zoned pseudotachylyte.
Fig. S4. Microstructures of the recrystallized pseudotachylyte.
Fig. S5. BSEs of the growth on garnet clasts in the cataclasites.
Fig. S6. Ternary plots of garnet and diopside compositions associated with the fault.
Fig. S7. BSE of fragmented plagioclase in the damage zone.
Fig. S8. Pole figures of the microstructures analyzed with EBSD (Fig. 3).
Fig. S9. Grain size distribution of the garnet fragments with growth rims in the cataclasites (Figs. 2C and 3A).
Fig. S10. Asymmetric damage and shear along a neighboring fault.
Table S1. Average mineral compositions for garnet and diopside clasts and associated growth rims within the cataclasites.

REFERENCES AND NOTES

1. H. Austrheim, K. G. Dunkel, O. Plümper, B. Ildefonse, Y. Liu, B. Jamtveit, Fragmentation of wall rock garnets during deep crustal earthquakes. *Sci. Adv.* **3**, e1602067 (2017).
2. L. Menegon, G. Pennacchioni, N. Malaspina, K. Harris, E. Wood, Earthquakes as precursors of ductile shear zones in the dry and strong lower crust. *Geochem. Geophys. Geosyst.* **18**, 4356–4374 (2017).
3. A. Putnis, B. Jamtveit, H. Austrheim, Metamorphic processes and seismicity: The Bergen Arcs as a natural laboratory. *J. Petrol.* **58**, 1871–1898 (2017).
4. M. Scambelluri, G. Pennacchioni, M. Gilio, M. Bestmann, O. Plümper, F. Nestola, Fossil intermediate-depth earthquakes in subducting slabs linked to differential stress release. *Nat. Geosci.* **10**, 960–966 (2017).
5. B. Jamtveit, Y. Ben-Zion, F. Renard, H. Austrheim, Earthquake-induced transformation of the lower crust. *Nature* **556**, 487–491 (2018).
6. A. Petley-Ragan, K. G. Dunkel, H. Austrheim, B. Ildefonse, B. Jamtveit, Microstructural records of earthquakes in the lower crust and associated fluid-driven metamorphism in plagioclase-rich granulites. *J. Geophys. Res. Solid Earth* **123**, 3729–3746 (2018).
7. F. Hawemann, N. S. Mancktelow, G. Pennacchioni, S. Wex, A. Camacho, Weak and slow, strong and fast: how shear zones evolve in a dry continental crust (Musgraves, Ranges, Central Australia). *J. Geophys. Res. Solid Earth* **124**, 219–240 (2018).
8. S. Braeck, Y. Y. Podladchikov, Spontaneous thermal runaway as an ultimate failure mechanism of materials. *Phys. Rev. Lett.* **98**, 095504 (2007).
9. T. John, S. Medvedev, L. H. Rüpke, T. B. Andersen, Y. Y. Podladchikov, H. Austrheim, Generation of intermediate-depth earthquakes by self-localizing thermal runaway. *Nat. Geosci.* **2**, 137–140 (2009).
10. G. Hetényi, R. Cattin, F. Brunet, L. Bollinger, J. Vergne, J. L. Nábělek, M. Diament, Density distribution of the India plate beneath the Tibetan plateau: Geophysical and petrological constraints on the kinetics of lower-crustal eclogitization. *Earth Planet. Sci. Lett.* **264**, 226–244 (2007).
11. S. Incel, N. Hilairet, L. Labrousse, T. John, D. Deldicque, T. Ferrand, Y. Wang, J. Renner, L. Morales, A. Schubnel, Laboratory earthquakes triggered during eclogitization of lawsonite-bearing blueschist. *Earth Planet. Sci. Lett.* **459**, 320–331 (2017).

12. F. Shi, Y. Wang, T. Yu, L. Zhu, J. Zhang, J. Wen, J. Gasc, S. Incel, A. Schubnel, Z. Li, T. Chen, W. Liu, V. Prakapenka, Z. Jin, Lower-crustal earthquakes in southern Tibet are linked to eclogitization of dry metastable granulite. *Nat. Commun.* **9**, 3483 (2018).
13. H. Austrheim, Eclogitization of lower crustal granulites by fluid migration through shear zones. *Earth Planet. Sci. Lett.* **81**, 221–232 (1987).
14. B. Bingen, W. J. Davis, H. Austrheim, Zircon U-Pb geochronology in the Bergen arc eclogites and their Proterozoic protoliths, and implications for the pre-Scandian evolution of the Caledonides in western Norway. *GSA Bull.* **113**, 640–649 (2001).
15. B. Jamtveit, E. Moulas, T. B. Andersen, H. Austrheim, F. Corfu, A. Petley-Ragan, S. M. Schmalholz, High pressure metamorphism caused by fluid induced weakening of deep continental crust. *Sci. Rep.* **8**, 17011 (2018).
16. C. Aupart, K. G. Dunkel, L. Angheluta, H. Austrheim, B. Ildefonse, A. Malthe-Sørenssen, B. Jamtveit, Olivine grain size distributions in faults and shear zones: Evidence for nonsteady state deformation. *J. Geophys. Res. Solid Earth* **123**, 7421–7443 (2018).
17. O. Dor, Y. Ben-Zion, T. K. Rockwell, J. Brune, Pulverized rocks in the mojave section of the San Andreas Fault Zone. *Earth Planet. Sci. Lett.* **245**, 642–654 (2006).
18. T. M. Mitchell, Y. Ben-Zion, T. Shimamoto, Pulverized fault rocks and damage asymmetry along the Arima-Takatsuki Tectonic Line, Japan. *Earth Planet. Sci. Lett.* **308**, 284–297 (2011).
19. M. Rempe, T. Mitchell, J. Renner, S. Nippress, Y. Ben-Zion, T. Rockwell, Damage and seismic velocity structure of pulverized rocks near the San Andreas Fault. *J. Geophys. Res.* **118**, 2813–2831 (2013).
20. W. A. Sullivan, E. M. Peterman, Pulverized granite at the brittle-ductile transition: An example from the Kellyland fault zone, eastern Maine, U.S.A. *J. Struct. Geol.* **101**, 109–123 (2017).
21. T. Rockwell, M. Sisk, G. Girty, O. Dor, N. Wechsler, Y. Ben-Zion, Chemical and physical characteristics of pulverized Tejon Lookout granite adjacent to the San Andreas and Garlock faults: Implications for earthquake physics. *Pure Appl. Geophys.* **166**, 1725–1746 (2009).
22. N. Wechsler, E. E. Allen, T. K. Rockwell, G. Girty, J. S. Chester, Y. Ben-Zion, Characterization of pulverized granitoids in a shallow core along the San Andreas Fault, Littlerock, CA. *Geophys. J. Int.* **186**, 401–417 (2011).
23. J. Muto, T. Nakatani, O. Nishikawa, H. Nagahama, Fractal particle size distribution of pulverized fault rocks as a function of distance from the fault core. *Geophys. Res. Lett.* **42**, 3811–3819 (2015).
24. J. G. Spray, Pseudotachylyte controversy: Fact or friction? *Geology* **23**, 1119–1122 (1995).
25. J. F. Magloughlin, Microstructural and chemical changes associated with cataclasis and frictional melting at shallow crustal levels: The cataclasite-pseudotachylyte connection. *Tectonophysics* **204**, 243–260 (1992).
26. G. Di Toro, G. Pennacchioni, Fault plane processes and mesoscopic structure of a strong-type seismogenic fault in tonalites (Adamello batholith, Southern Alps). *Tectonophysics* **402**, 55–80 (2005).
27. W. A. Griffith, T. M. Mitchell, J. Renner, G. Di Toro, Coseismic damage and softening of fault rocks at seismogenic depths. *Earth Planet. Sci. Lett.* **353–354**, 219–230 (2012).
28. V. Lyakhovsky, Y. Ben-Zion, A. Ilchev, A. Mendecki, Dynamic rupture in a damage-breakage rheology model. *Geophys. J. Int.* **206**, 1126–1143 (2016).
29. N. Monzawa, K. Otsuki, Comminution and fluidization of granular fault materials: Implications for fault slip behavior. *Tectonophysics* **367**, 127–143 (2003).
30. C. G. Sammis, G. C. P. King, Mechanical origin of power law scaling in fault zone rock. *Geophys. Res. Lett.* **34**, L04312 (2007).
31. I. Kurzon, V. Lyakhovsky, Y. Ben-Zion, Dynamic rupture and seismic radiation in a damage–breakage rheology model. *Pure Appl. Geophys.* **176**, 1003–1020 (2019).
32. L. B. Freund, *Dynamic Fracture Mechanics* (Cambridge Univ. Press, Cambridge, 1990).
33. C. H. Scholz, N. H. Dawers, J.-Z. Yu, M. H. Anders, P. A. Cowie, Fault growth and fault scaling laws: Preliminary results. *J. Geophys. Res.* **98**, 21951–21961 (1993).
34. D. J. Andrews, Rupture dynamics with energy loss outside the slip zone. *J. Geophys. Res.* **110**, B01307 (2005).
35. Y. Ben-Zion, Z. Shi, Dynamic rupture on a material interface with spontaneous generation of plastic strain in the bulk. *Earth Planet. Sci. Lett.* **236**, 486–496 (2005).
36. G. Di Toro, S. Nielsen, G. Pennacchioni, Earthquake rupture dynamics frozen in exhumed ancient faults. *Nature* **436**, 1009–1012 (2005).
37. Z. Reches, T. A. Dewers, Gouge formation by dynamic pulverization during earthquake rupture. *Earth Planet. Sci. Lett.* **235**, 361–374 (2005).
38. W. A. Griffith, A. Rosakis, D. D. Pollard, C. W. Ko, Dynamic rupture experiments elucidate tensile crack development during propagating earthquake ruptures. *Geology* **37**, 795–798 (2009).
39. S. Xu, Y. Ben-Zion, Theoretical constraints on dynamic pulverization of fault zone rocks. *Geophys. J. Int.* **209**, 282–296 (2017).
40. Y. Ben-Zion, J.-P. Ampuero, Seismic radiation from regions sustaining material damage. *Geophys. J. Int.* **178**, 1351–1356 (2009).
41. H. R. Wenk, Are pseudotachylites products of fracture or fusion? *Geology* **6**, 507–511 (1978).
42. S. Papa, G. Pennacchioni, R. J. Angel, M. Faccenda, The fate of garnet during (deep-seated) coseismic frictional heating: The role of thermal shock. *Geology* **46**, 471–474 (2018).
43. D. L. Wells, K. J. Coppersmith, New empirical relationships among magnitude, rupture length, rupture width, rupture area, and surface displacement. *Bull. Seismol. Soc. Am.* **84**, 974–1002 (1994).
44. Y. Ben-Zion, Collective behavior of earthquakes and faults: Continuum-discrete transitions, progressive evolutionary changes, and different dynamic regimes. *Rev. Geophys.* **46**, RG4006 (2008).
45. J. R. Rice, C. G. Sammis, R. Parsons, Off-fault secondary failure induced by a dynamic slip pulse. *Bull. Seismol. Soc. Am.* **95**, 109–134 (2005).
46. Y. Ben-Zion, Dynamic ruptures in recent models of earthquake faults. *J. Mech. Phys. Solids* **49**, 2209–2244 (2001).
47. A. Clerc, F. Renard, H. Austrheim, B. Jamtveit, Spatial and size distributions of garnets grown in a pseudotachylyte generated during a lower crust earthquake. *Tectonophysics* **733**, 159–170 (2018).

Acknowledgments: We thank C. Nevado and D. Delmas for high-quality thin-section polishing, F. Barou for the EBSD measurements, B. Cordonnier for the acquisition of the x-ray tomography data, W. A. Griffith for providing suggestions on an early version of the manuscript, and two anonymous reviewers for their very thorough reviews that improved our paper. **Funding:** This project has been supported by the European Research Council (ERC) Advanced Grant Agreement 669972 "Disequilibrium Metamorphism" ("DIME") to B.J., the Norwegian Research Council grant 250661 to F.R., and the Natural Science and Engineering Research Council (NSERC) of Canada Postgraduate Scholarship Doctoral (PGS-D) 489392 to A.P.-R. **Author contributions:** B.J., Y.B.-Z., and F.R. designed the project. A.P.-R., B.J., and H.A. collected the samples and field data. A.P.-R. analyzed the thin sections, obtained the grain size distributions, and analyzed the EBSD data. B.I. aided in the acquisition and analysis of the EBSD data. The fault illustration in Fig. 4 was drafted by Y.B.-Z. and digitized by A.P.-R. The manuscript was written by A.P.-R. and B. J. with contributions from the other authors. **Competing interests:** The authors declare that they have no competing interests. **Data and materials availability:** All data needed to evaluate the conclusions in the paper are present in the paper and/or the Supplementary Materials. Additional data related to this paper may be requested from the authors. The EBSD data, BSE images used for image analysis and XR-CT data are available online at Open Science Forum (https://osf.io/sm8qy/).

Submitted 16 November 2018
Accepted 25 June 2019
Published 31 July 2019
10.1126/sciadv.aaw0913

Citation: A. Petley-Ragan, Y. Ben-Zion, H. Austrheim, B. Ildefonse, F. Renard, B. Jamtveit, Dynamic earthquake rupture in the lower crust. *Sci. Adv.* **5**, eaaw0913 (2019).

Dynamic earthquake rupture in the lower crust

Arianne Petley-Ragan, Yehuda Ben-Zion, Håkon Austrheim, Benoit Ildefonse, François Renard and Bjørn Jamtveit

Sci Adv **5** (7), eaaw0913.
DOI: 10.1126/sciadv.aaw0913